

NICER observations of the black hole candidate MAXI J0637–430 during the 2019-2020 Outburst

Arghajit Jana^{1*}, Gaurava K. Jaisawal², Sachindra Naik¹, Neeraj Kumari^{1,3},
Birendra Chhotaray^{1,3}, Diego Altamirano⁴, Ronald A. Remillard⁵, Keith C. Gendreau⁶

¹*Astronomy & Astrophysics Division, Physical Research Laboratory, Navrangpura, Ahmedabad, 380009, India*

²*National Space Institute, Technical University of Denmark, Elektrovej, 327-328, DK-2800 Lyngby, Denmark*

³*Indian Institute of Technology, Gandhinagar - 382355, Gujarat, India*

⁴*School of Physics and Astronomy, University of Southampton, Southampton, SO17 1BJ, UK*

⁵*MIT Kavli Institute for Astrophysics and Space Research, MIT, 70 Vassar Street, Cambridge, MA 02139, USA*

⁶*Astrophysics Science Division, NASA Goddard Space Flight Center, Greenbelt, MD 20771, USA*

Accepted XXX. Received YYY; in original form ZZZ

ABSTRACT

We present detailed timing and spectral studies of the black hole candidate MAXI J0637–430 during its 2019-2020 outburst using observations with the *Neutron Star Interior Composition Explorer* (NICER) and the *Neil Gehrels Swift Observatory*. We find that the source evolves through the soft-intermediate, high-soft, hard-intermediate and low-hard states during the outburst. No evidence of quasi-periodic oscillations is found in the power density spectra of the source. Weak variability with fractional rms amplitude $< 5\%$ is found in the softer spectral states. In the hard-intermediate and hard states, high variability with the fractional rms amplitude of $> 20\%$ is observed. The 0.7 – 10 keV spectra with NICER are studied with a combined disk-blackbody and nthcomp model along with the interstellar absorption. The temperature of the disc is estimated to be 0.6 keV in the rising phase and decreased slowly to 0.1 keV in the declining phase. The disc component was not detectable or absent during the low hard state. From the state-transition luminosity and the inner edge of the accretion flow, we estimate the mass of the black hole to be in the range of 5 – 12 M_{\odot} , assuming the source distance of $d < 10$ kpc.

Key words: X-Rays:binaries – stars: individual: (MAXI J0637–430) – stars:black holes – accretion, accretion discs

1 INTRODUCTION

An X-ray binary (XRB) consists of a normal star and a compact object. The compact object can be a black hole (BH), or a neutron star (NS). Depending on the mass of the companion star, the XRBs can be classified as a high mass X-ray binary (HMXB) or a low mass X-ray binary (LMXB) (White et al. 1995; Remillard & McClintock 2006). An HMXB system contains an O- or B-type companion star, while an LMXB contains an A-type or later star (Tetarenko et al. 2016). A transient XRB spends most of the time in the quiescent state during which the compact object is marginally detectable or even non-detectable with the current generation X-ray detectors. The transient XRBs occasionally show X-ray outbursts that last for several weeks to months. During the outburst, the X-ray luminosity of the source increases by several orders of magnitude compared to the quiescent state.

A spectrum of a black hole X-ray binary (BHXR) can be

approximated with a soft thermal multi-colour blackbody component and a non-thermal power-law component. The multi-colour blackbody component originates from a standard thin accretion disc (Shakura & Sunyaev 1973; Novikov & Thorne 1973). In contrast, the power-law component originates in a Compton cloud located close to the BH (Sunyaev & Titarchuk 1980, 1985). The soft X-ray photons originated from the standard accretion disc undergo inverse-Comptonization in the Compton cloud and produce the hard power-law component (Haardt & Maraschi 1993; Zdziarski et al. 1993; Titarchuk 1994; Chakrabarti & Titarchuk 1995; Życki et al. 1999; Done et al. 2007).

An outbursting BHXR shows rapid variation and fluctuation in spectral and timing properties (Méndez & van der Klis 1997; van der Klis 1989, 2000). A correlation between the spectral and timing properties of the source can be seen in the hardness–intensity diagram (HID; Homan et al. 2001; Homan & Belloni 2005; Nandi et al. 2012), accretion rate–intensity diagram (ARRID; Jana et al. 2016), rms–intensity diagram (RID; Muñoz-Darias et al. 2011), or hardness–rms diagram (HRD; Belloni et al. 2005). In gen-

* E-mail: argha@prl.res.in

eral, an outbursting BHXRB exhibits four different spectral states, viz. low hard state (LHS), hard-intermediate state (HIMS), soft-intermediate state (SIMS) and high soft state (HSS), and evolves as LHS \rightarrow HIMS \rightarrow SIMS \rightarrow HSS \rightarrow SIMS \rightarrow HIMS \rightarrow LHS (Remillard & McClintock 2006; Nandi et al. 2012; Jana et al. 2020). A BHXRB also shows low-frequency quasi-periodic oscillations (LFQPOs) in the power density spectra (PDS) observed in a range of 0.1–20 Hz. A LFQPO can be classified as type-A, type-B or type-C depending on the Q-value of the QPO ($Q = \nu / \Delta\nu$, ν and $\Delta\nu$ are centroid QPO frequency and full-width-half-maxima, respectively), nature of broadband noise, and rms amplitude of the QPO & broad noise (Casella et al. 2005, and references therein).

Each spectral state is characterized by different spectral and timing properties (for a review, see; Remillard & McClintock 2006). The LHS is characterized by a cool disc of temperature in $\sim 0.2 - 0.5$ keV range and photon index, $\Gamma \sim 1.5 - 1.7$. Sometimes, the disc component is not detectable in this state. In general, the hard X-ray photon flux dominates over the soft X-ray photon flux. Evolving type-C QPO is observed in this state. Along with the QPO, broadband noise and rms amplitude of $\sim 20 - 40\%$ are observed in the PDS of the source. A compact and quasi-stable jet is also observed in the LHS (Fender & Belloni 2004). In the HIMS, the soft photon flux increases relative to the hard photon flux. The source spectra became steep with a photon index, $\Gamma \sim 2$. Evolving type-C QPO is also observed in this state. The SIMS is associated with $\Gamma \sim 2.2 - 2.5$, with high soft photon flux. Sporadic type-A or type-B QPOs are observed in this state. The SIMS is often associated with a discrete ejection or blobby jets. The HSS is dominated by the disc flux or soft X-ray photon flux, with temperature $T \sim 1$ keV. The spectra are observed to be steep with $\Gamma \geq 2.5$. No QPO is observed in this state. A weak broadband noise with rms amplitude $< 5\%$ is observed in this state. No jet is observed in the HSS (Fender & Belloni 2004).

The black hole candidate (BHC) MAXI J0637–430 was discovered with *MAXI/GSC* on 2 November 2019 during the onset of the 2019–2020 X-ray outburst (Negoro et al. 2019). The outburst continued for ~ 6 months. The *Swift/XRT* observation of the field localized the source at RA/Dec(J2000) = 99.09828°, -42.8678° (Kennea et al. 2019). After the discovery, the source was observed in optical (Li & Kong 2019), infrared (Murata et al. 2019), and radio wavelengths (Russell et al. 2019). Several X-ray satellites such as *NICER* (Remillard et al. 2020), *AstroSAT* (Thomas et al. 2019), and *NuSTAR* (Tomsick et al. 2019) also reported the primary timing and spectral analysis of the source. Preliminary studies suggest that the source is an LMXB (Strader et al. 2019) hosting a BH as the compact object (Tomsick et al. 2019).

In this paper, we present our studies on the 2019–2020 X-ray outburst of MAXI J0637–430 using data from the *NICER* and *Swift* observatories. The paper is organized in the following way. In §2, we describe the observation and data analysis processes. The results obtained from our timing and spectral analysis are presented in §3. In §4, we discuss our findings and finally, in §5, we summarize our results.

2 OBSERVATION AND DATA ANALYSIS

2.1 *NICER*

Soon after its discovery, the BHC MAXI J0637–430 was observed with *NICER* at several epochs between 3 November 2019 and 9 April 2020. *NICER* is an attached external payload on the International Space Station that offers an X-ray timing instrument (XTI;

Gendreau et al. 2012) working in the 0.2–12 keV photon energy range. The XTI consists of 56 X-ray “concentrator” optics, each associated with a silicon drift detector (Prigozhin et al. 2012). There are 52 active detectors, providing a total effective area of 1900 cm² at 1.5 keV. The timing resolution of *NICER* is ~ 100 ns, whereas the spectral resolution is ~ 85 eV at 1 keV. We used a total of 88 epochs of observations under the IDs 22009501xx and 32009501xx (see Table 1) with a total exposure time of ≈ 137 ks to study the nature of the BHC MAXI J0637–430 during its 2019–2020 X-ray outburst. The data were reprocessed with the `nicer12`¹ script in the presence of the latest gain and calibration files of version 20200722. Standard GTIs were also generated using the `nimaketime` task. The reprocessed cleaned events were used for extracting the light curves and spectra in the XSELECT environment of FT00LS. Ancillary response file and response matrix file of version 20200722 are considered in our spectral analysis. The background corresponding to each epoch of the observations is simulated by using the `nibackgen3C50`² tool (Remillard et al., in prep.).

The 0.5 – 10 keV light curves were created at a 400 μ s time bin. Power density spectra (PDS) were generated by applying the Fast Fourier Transformation (FFT) technique on the light curves using `powspec` task of FT00LS. We divided the light curves into 8192 intervals and computed the Poisson noise subtracted PDS for each interval. Then, we averaged all the PDS to obtain the final PDS for each observation. The final PDS are normalized to give the fractional rms spectra in $(rms/mean)^2 Hz^{-1}$ unit. Then, we re-binned the PDS with a factor of 1.05.

For the spectral study, we used data in the energy range of 0.7–10 keV. The spectra were re-binned to have a minimum of 20 counts per bin. Data below 0.7 keV are not included in our spectral fitting due to observed calibration issues like excess at lower energies. We added a systematic of 1.5% during the spectral analysis, as recommended by the *NICER* team³ (Jaisawal et al. 2019).

2.2 *Swift*

The *Swift/XRT* observed MAXI J0637–430 several times between 7 November 2019 and 10 June 2020. We used a total of 85 epochs of observations, observed between 7 November 2019 and 30 March 2020. The *Swift/XRT* observations were carried out in both window-timing (WT) and photon counting (PC) mode, under the IDs 0001217, and 00088999 with a total exposure time of ~ 100 ks. The 0.5 – 10 keV spectra were generated using the standard online tools provided by the UK *Swift* Science Data Centre (Evans et al. 2009)⁴. For the present study, we used both WT and PC mode spectra and light curves in the energy band of 0.5 – 10 keV.

3 RESULT

3.1 Outburst Profile

Following the discovery, MAXI J0637–430 was extensively observed with *NICER* and *Swift/XRT*. In Fig. 1, we show the evolution of the 0.5 – 10 keV *NICER* light curve in counts s⁻¹ (panel-a), the 0.5 – 10 keV *Swift/XRT* flux in 10⁻¹⁰ erg cm⁻² s⁻¹ (panel-b), and the 2–20 keV *MAXI/GSC* count rate in photons cm⁻² s⁻¹ (panel-c).

¹ https://heasarc.gsfc.nasa.gov/docs/nicer/analysis_threads/nicer12/

² https://heasarc.gsfc.nasa.gov/docs/nicer/toolsnicer_bkg_est_tools.html

³ https://heasarc.gsfc.nasa.gov/docs/nicer/data_analysis/nicer_analysis.html

⁴ http://www.swift.ac.uk/user_objects/

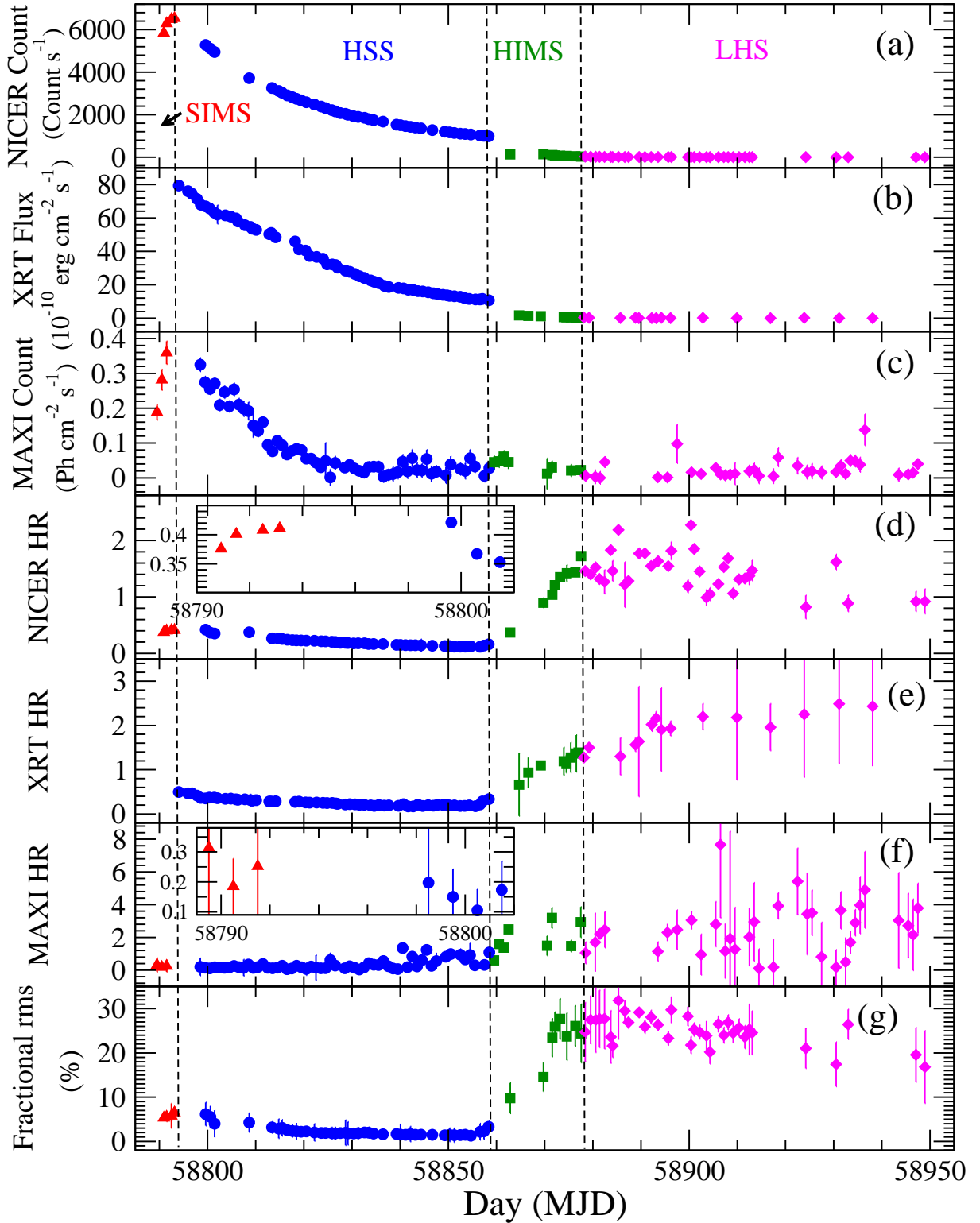


Figure 1. The variation of (a) 0.5 – 10 keV *NICER* count rate in counts s^{-1} , (b) 0.5 – 10 keV *Swift*/*XRT* flux in 10^{-10} erg cm^{-2} s^{-1} , (c) 2 – 20 keV *MAXI*/*GSC* count rate in photons cm^{-2} s^{-1} , (d) *NICER* hardness ratio (HR-1), (e) *Swift*/*XRT* hardness ratio (HR-2), and (f) *MAXI*/*GSC* hardness ratio (HR-3) are shown with days (in MJD). In panel (g), the evolution of 0.1 – 50 Hz fractional rms amplitude in the 0.5 – 10 keV energy band, obtained from *NICER* observation, is shown. The red triangles, blue circles, green squares, and magenta diamond indicate SIMS, HSS, HIMS, and LHS, respectively, during the outburst. The vertical dashed lines separates different spectral states.

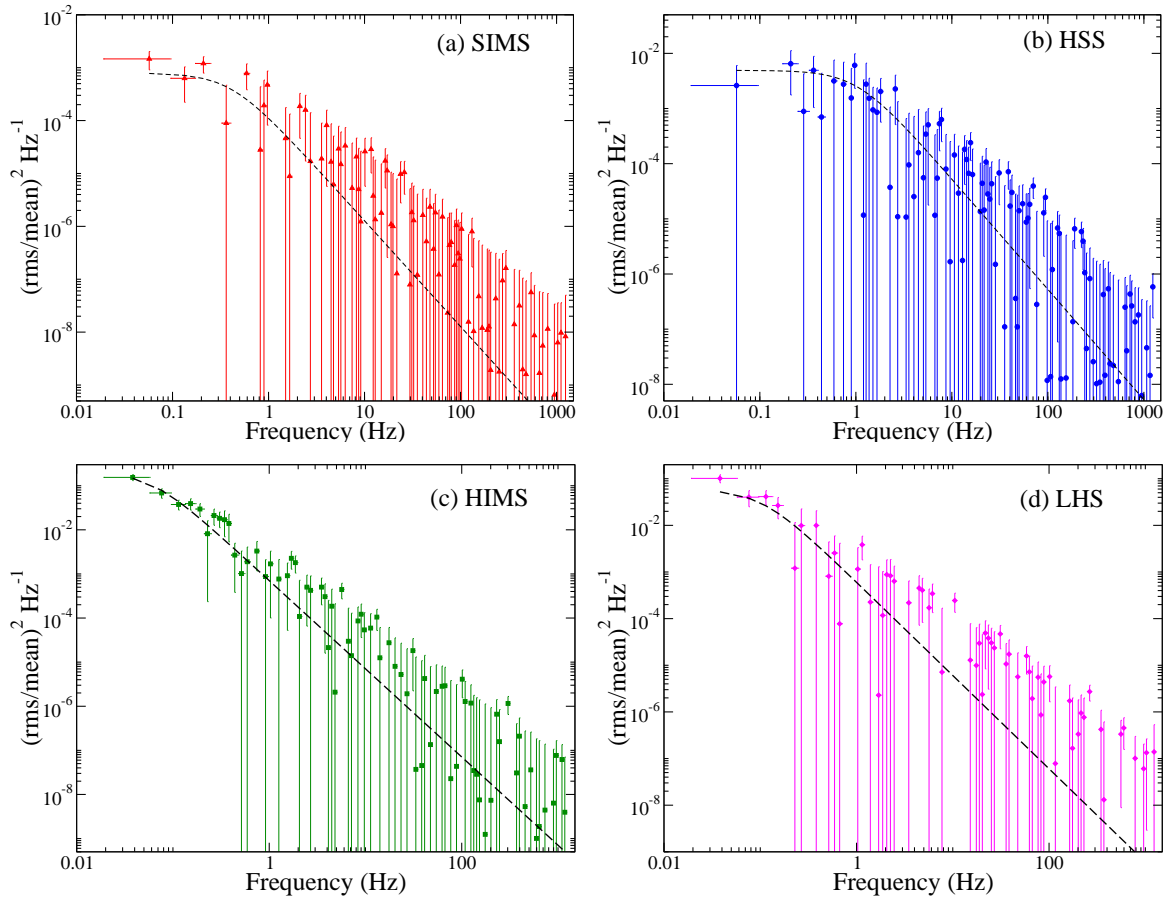


Figure 2. Power density spectra obtained from the *NICER* observations on (a) 2019 November 4 (Obs ID : 2200950102), (b) 2020 January 2 (Obs ID: 2200950145), (c) 2020 February 10 (Obs ID: 2200950173), and (d) 2020 March 2 (Obs ID: 3200950102). The PDS are fitted with Lorentzian function. The dashed lines represent the best-fit Lorentzian.

The hardness ratios obtained from the *NICER* observations (panel-d), *Swift*/XRT observations (panel-e) and *MAXI*/GSC observations (panel-f) are shown in Fig 1. The 0.01 – 50 Hz fractional rms amplitude (r) in 0.5 – 10 keV energy band, obtained from the *NICER* observations during the outburst, is also shown in the bottom panel (panel-g) of Fig 1. The insets in panels-d & f represent the magnified version of the hardness ratios from the *NICER* and *MAXI*/GSC observations during the peak of the outburst. The hardness ratio (HR) for the *NICER* observations is obtained by taking ratio between the count rates in 2 – 10 keV and 0.5 – 2 keV energy bands. For the *Swift*/XRT observations, the HR is defined as the ratio between the 2 – 10 keV flux and 0.5 – 2 keV flux. For *MAXI*/GSC observations, the HR is defined as the ratio between the count rates in 4 – 20 keV and 2 – 4 keV energy bands.

As mentioned earlier, *NICER* started observing the source one day after the discovery, i.e. from 3 November 2019 (MJD 58790.92). The X-ray intensity of the source rapidly increased and became maximum on 6 November 2019 (MJD 58793.14) with a count rate of $6533 \text{ count s}^{-1}$ (Fig. 1(a)). After reaching the peak on 6 November 2019, the source entered the declining phase of the outburst. *Swift*/XRT started observing the source from 7 November 2019 (MJD 58794.03), when the source was already in the declining phase (Fig. 1(b)). From this day, the X-ray intensity gradually decreased up to 10 January 2020 (MJD 58858.37). After this, the X-ray intensity suddenly decreased by ~ 10 times on 14 January 2020 (MJD 58862.85) followed by a gradual decrease (Fig. 1(a) &

(b)). After that, the source faded toward the quiescent state. The 0.5 – 10 keV *Swift*/XRT flux and 2 – 20 keV *MAXI*/GSC count rate also showed similar variation. From the top three panels of Fig. 1, the outburst can be classified as the fast-rise-exponential decay type (Chen et al. 1997).

We observed that the *NICER* HR increased gradually in the rising phase of the outburst (inset figure in Fig. 1(d)) and reached the maximum on 12 November 2019 with HR ~ 0.4 . After that, the HR decreased slowly and became steady at a value of ~ 0.12 , till 10 January 2020 (MJD 58858.37). From 14 January 2020, the HR increased again until 29 January 2020 (MJD 58877.58) and remained high (in the range of 1 and 2) till the end of the observations. The HR obtained from the *Swift*/XRT and *MAXI*/GSC observations also showed similar behaviour. From the evolution of the HRs obtained from three instruments and fluxes in the soft and hard X-ray bands, we classified the entire outburst in four spectral states as marked in different colours and symbols in Fig 1 : soft-intermediate state (SIMS - marked in red triangles) in the rising phase, high soft state (HSS - marked in blue circles), hard-intermediate state (HIMS - marked in green squares) in the declining phase, and low hard state (LHS - marked as magenta diamonds).

3.2 Power Density Spectra

The PDS are generated from all *NICER* light curves to investigate the characteristics of the profiles. The light curves with $400 \mu\text{s}$

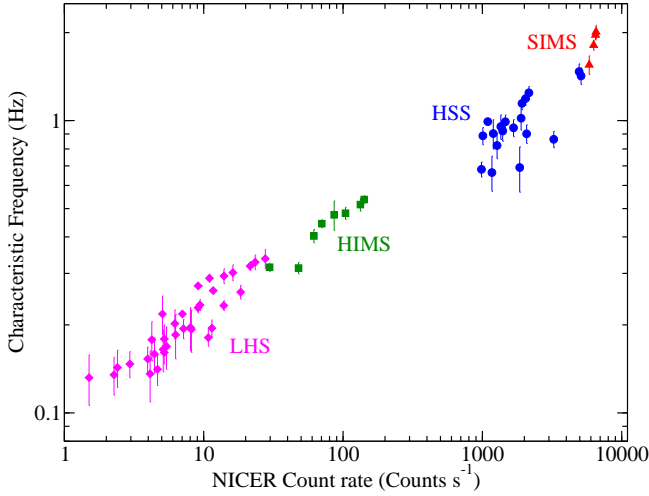


Figure 3. The characteristic frequency (ν_c) of broadband noise component is plotted as a function of 0.5 – 10 keV *NICER* count rate. The colours and symbol correspond to the different spectral states of the source during the outburst as described in Fig. 1.

time resolution allowed us to search for the QPO features in the PDS up to a maximum frequency of 1250 Hz. Representative PDS obtained from the *NICER* observations on 4 November 2019 (Obs ID : 2200950102, panel-a), 2 January 2020 (Obs ID: 2200950145, panel-b), 10 February 2020 (Obs ID: 2200950173, panel-c) and 2 March 2020 (Obs ID: 3200950102, panel-d) are shown in Fig. 2. We calculated the fractional rms amplitude (r) of the PDS by integrating the power in 0.01 – 50 Hz range (van der Klis 2004). We fitted the PDS with multiple Lorentzian functions. Most of the PDS in the SIMS and HSS were found to be fitted with a single zero-centroid Lorentzian, while more than one Lorentzian functions were required to fit the PDS in the HIMS and LHS. We calculated the characteristic frequency (ν_c) of the broadband noise for those observations. The characteristic frequency is the frequency where the component contributes the most of its variance per frequency and given by, $\nu_c = \sqrt{\nu_0 + (\Delta\nu/2)^2}$, where ν_0 and $\Delta\nu$ are the centroid frequency and full-width-half maxima, respectively (Nowak 2000; Belloni et al. 2002).

We searched for QPO in the PDS and found none. Thus, we tried to estimate the upper limit of the QPO. We found peaked noise in the PDS with an upper limit (UL) of rms < 5% at 1σ confidence level in five observations. As those peaked noises were detected at < 1σ level, we discard these band-limited peaked noises as QPO. We also tried to find QPO by combining the PDS from several observations in a particular state. However, we did not detect any evidence of QPO. We plotted the characteristic frequency as a function of 0.5 – 10 keV *NICER* count rate and found that they are correlated. We found weak red noise in the rising phase of the outburst ($r \sim 5\%$). The strength of the signal monotonically decreased to $r \sim 1\%$ in the declining phase until 10 January 2010 (MJD 58858.37). After that, the fractional rms amplitude increased to $r \sim 23\%$ on 23 January 2020. Then, the fractional rms amplitude varied within $r \sim 20-30\%$ till the end of the outburst (see Fig. 1g). In this phase, the PDS showed weak flat-top noise.

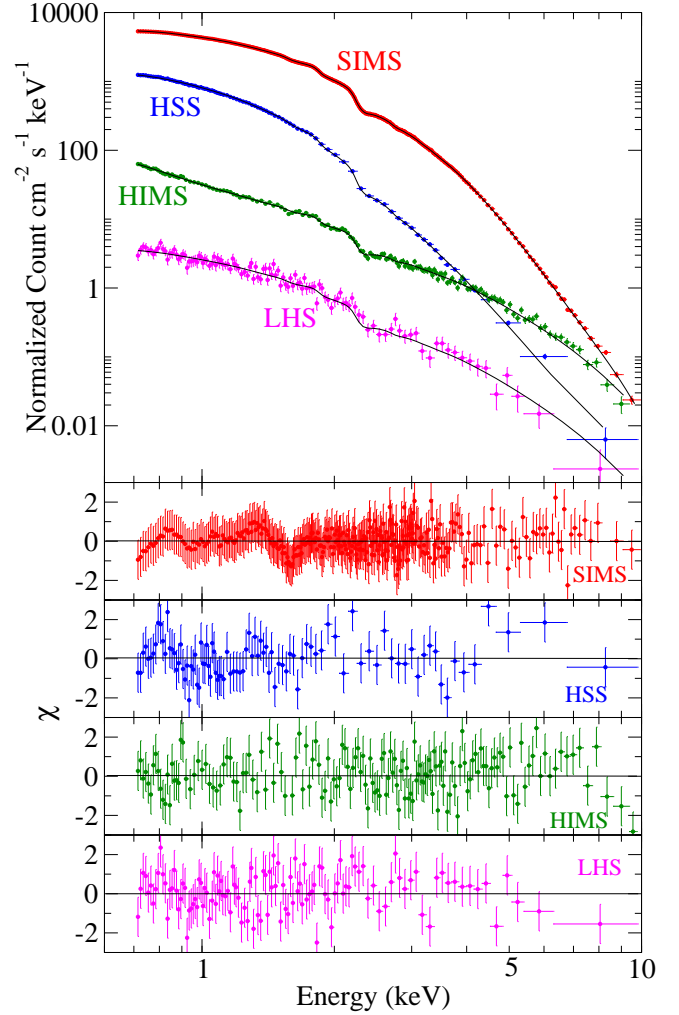


Figure 4. Energy spectra of MAXI J0637–430, obtained from the *NICER* observations at four different phases of the outburst, are shown in the top panel. Corresponding residuals obtained by fitting the spectra with disk blackbody and power law model, along with the interstellar absorption, are shown in the bottom panels. Red triangles, blue circles, green squares, and magenta diamonds correspond to the spectra observed on 4 November 2019 (Obs ID: 2200950102 – SIMS in the rising phase), 2 January 2020 (Obs ID: 2200950145 – HSS), 10 February 2020 (Obs ID: 2200950173 – HIMS in the declining phase) and 2 March 2020 (Obs ID: 3200950102 – LHS in the declining phase), respectively. In the upper panel, the black lines represent the best-fit model.

3.3 Spectral Properties

We carried out spectral studies of the BHC MAXI J0637–430 during its 2019–2020 X-ray outburst using the data from *NICER* and *Swift* observations. A total of 88 *NICER* and 85 *Swift*/XRT spectra were analyzed in our work. The spectral fitting was carried out in 0.7–10 keV energy band using HEASARC’s spectral analysis software package XSPEC v12.10⁵ (Arnaud 1996). The source and the background spectra were extracted by following mission-specific standard procedures, as described in Section 2. Appropriate effective area files and response matrices were used in the spectral fitting. We attempted to fit each spectrum with an absorbed pow-

⁵ <https://heasarc.gsfc.nasa.gov/docs/xanadu/xspec/>

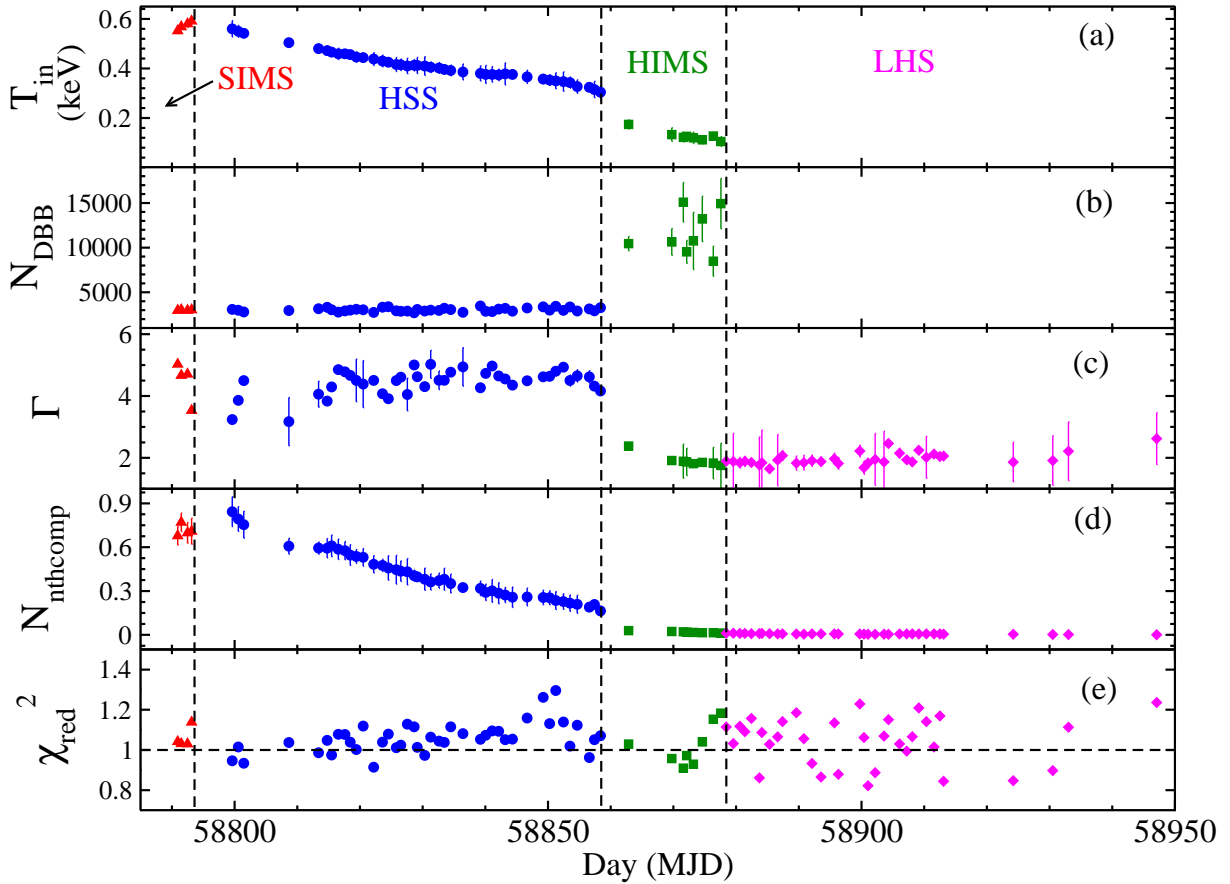


Figure 5. The evolution of (a) the inner disc temperature (T_{in} , in keV), (b) the diskbb normalization (N_{DBB}), (c) the photon index (Γ), (d) the nthcomp normalization (N_{nthcomp}), and (e) the reduced- χ^2 ($\chi_{\text{red}}^2 = \chi^2/\text{dof}$) are shown. The colours and symbol correspond to the different spectral states of the source during the outburst as described in Fig. 1. The vertical dashed lines separate different spectral states.

erlaw model. While fitting, the presence of positive residuals in soft X-ray ranges, specifically in the rising and initial part of the decaying phase of the outburst, allowed us to add a multi-colour blackbody component (Mitsuda et al. 1984; Makishima et al. 1986) with the absorbed powerlaw model. The model read in XSPEC as `tbabs(diskbb+powerlaw)`. In our fitting, the `tbabs` component with `wilm` abundances (Wilms et al. 2000) and cross-section of Verner et al. (1996) were used for examining the effect of interstellar absorption. The value of the hydrogen column density (N_{H}) was found to vary in the range of $(0.5 - 1.8) \times 10^{21} \text{ cm}^{-2}$. As the hydrogen column density in the direction of the source is likely to be constant during the outburst, the observed wide range of variation of N_{H} can be due to the effect of `powerlaw` continuum model spectral fittings. Thus, we replaced the `powerlaw` continuum model with the more robust `nthcomp` model (Życki et al. 1999). This model read as `tbabs(diskbb+nthcomp)` in XSPEC. During fitting, we linked the seed photon temperature (T_{bb}) of the `nthcomp` model with the inner disc temperature (T_{in}) of the `diskbb` component. We also fixed the Compton corona temperature (kT_{e}) at 1000 keV as it is expected to be beyond the *NICER* energy range. With this model, we observed that the N_{H} varied in a narrow range of $(1 - 6) \times 10^{20} \text{ cm}^{-2}$. Then, we attempted to fit all 88 observations simultaneously with N_{H} linked across the spectra. The simultaneous fitting gave us a good-fit with $\chi^2 = 28805$ for 25336 dof ($\chi_{\text{red}}^2 = 1.136$, for 88 observations). We obtained $N_{\text{H}} = (5.04 \pm 0.52) \times 10^{20} \text{ cm}^{-2}$ from

the simultaneous fitting which is consistent with the Galactic value of $N_{\text{H}} = 5.2 \times 10^{21} \text{ cm}^{-2}$ (HI4PI Collaboration et al. 2016). Thus, we fixed the hydrogen column density at the Galactic value during our analysis.

Four representatives *NICER* spectra at different epochs of the outburst are shown in the top panel of Fig. 4. The residuals obtained from the spectral fitting with the above model are presented in the bottom panels of Fig. 4. While fitting, we noticed that the thermal disc component was only required in the first 54 *NICER* observations. Beyond 29 January 2020 (MJD 58877.58), the multi-colour disc blackbody component was so faint that it was not detected in the spectral fitting. To check whether the `diskbb` component was required in the spectral fitting, we ran FTTOOLS task `ftest` and found that the `diskbb` component was not required. Nonetheless, the UL on the disc flux in the LHS was estimated to be $\leq 10^{-14} \text{ erg cm}^{-2} \text{ s}^{-1}$, which is less than 1% of the Comptonized flux. Therefore, the spectra beyond 29 January 2020 were fitted with an absorbed `nthcomp` model only. Both the models, an absorbed `nthcomp` model with thermal component (for spectra till 29 January 2020) and without thermal component (for spectra beyond 29 January 2020), provided a good fit with the χ_{red}^2 values close to 1. The evolution of various spectral parameters such as (a) the inner disc temperature (T_{in}), (b) the `diskbb` normalization (N_{DBB}), (c) the photon indices (Γ), and (d) the `nthcomp` normalization are shown in Fig. 5. In the rising phase of the outburst (red triangles), the inner disc temperature (T_{in}) was maximum and in the range of

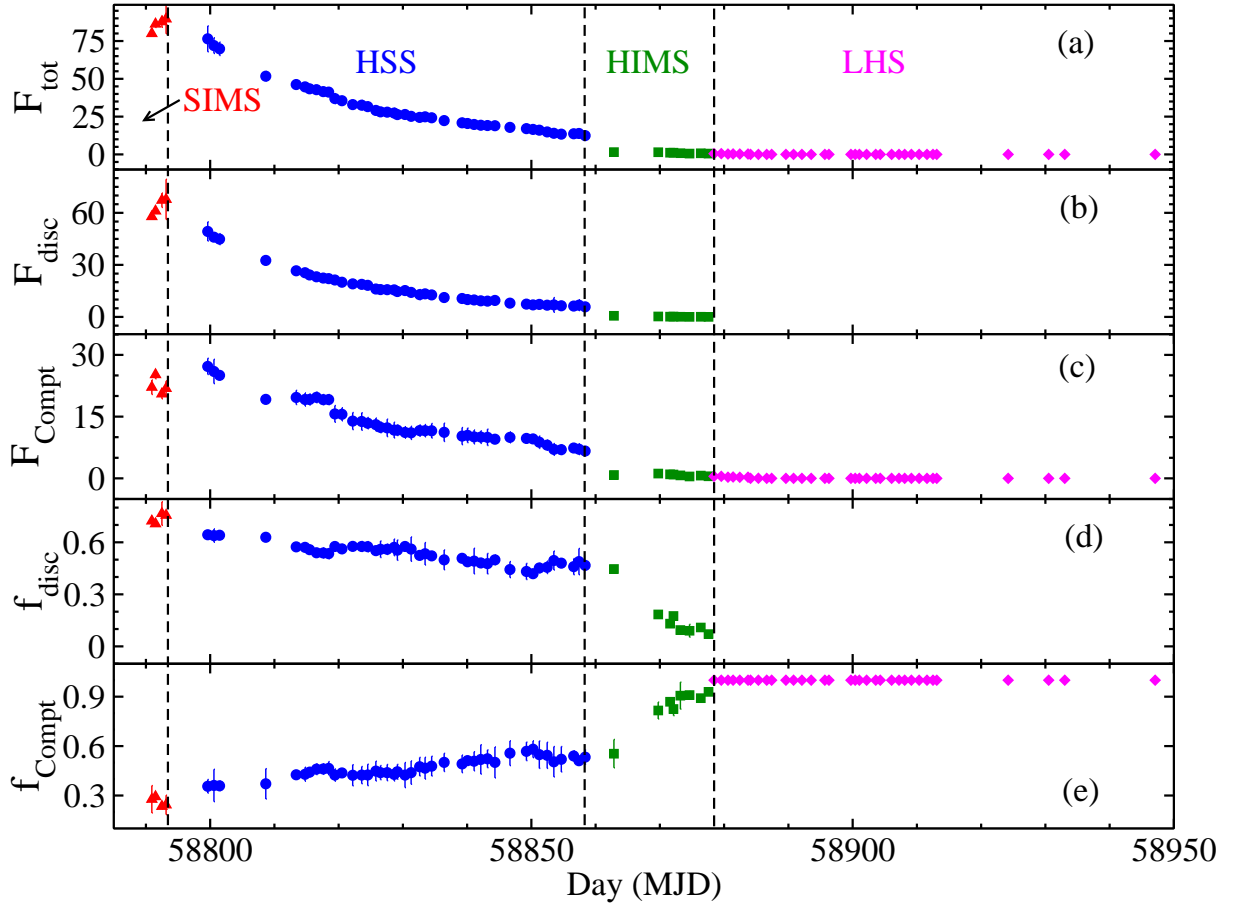


Figure 6. The changes in the (a) 0.7 – 10 keV unabsorbed flux, (b) 0.7 – 10 keV thermal disc flux (F_{disc}), (c) 0.7 – 10 keV non-thermal Comptonized flux (F_{Compt}), (d) thermal fraction (f_{disc}), and (e) non-thermal Comptonized fraction (f_{Compt}) are shown. The fluxes are in the unit of 10^{-10} erg cm^{-2} s^{-1} . Thermal and non-thermal fractions are defined as $f_{\text{disc}} = F_{\text{disc}}/F_{\text{tot}}$, and $f_{\text{Compt}} = F_{\text{Compt}}/F_{\text{tot}}$, respectively. The colours and symbol correspond to the different spectral states of the source during the outburst as described in Fig. 1. The vertical dashed lines separate different spectral states.

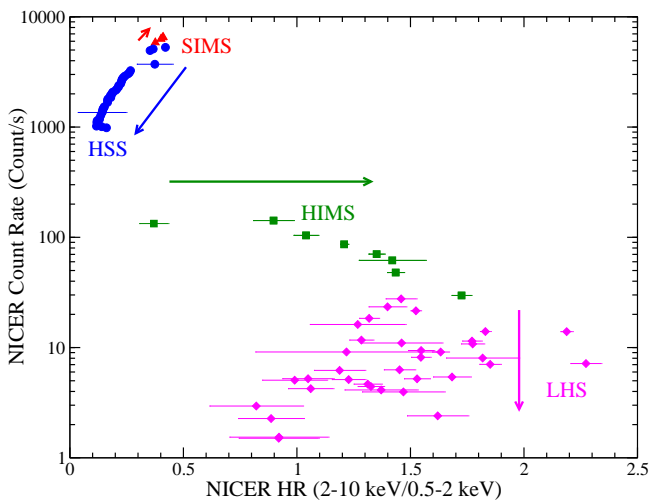


Figure 7. The hardness ratio – intensity diagram (HID) obtained from the 0.5 – 10 keV *NICER* observations of MAXI J0637–430 is shown. The colours and symbol correspond to the different spectral states of the source during the outburst as described in Fig. 1.

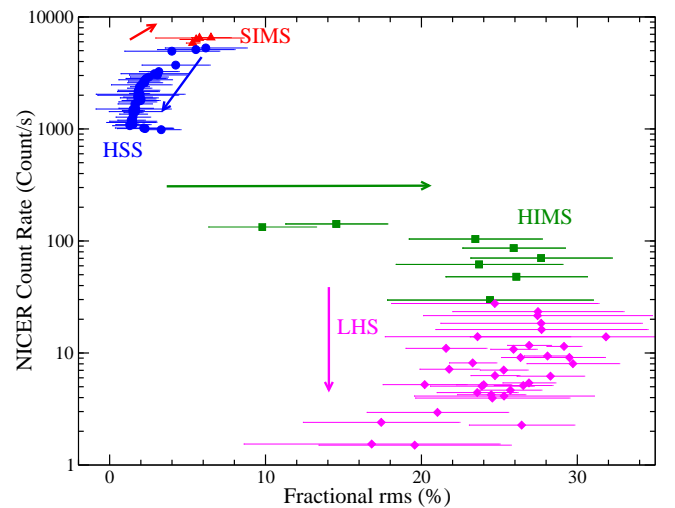


Figure 8. The rms–intensity diagram (RID) where the 0.5 – 10 keV count rate is plotted as a function of the 0.1 – 50 Hz fractional rms amplitude. The colours and symbol correspond to the different spectral states of the source during the outburst as described in Fig. 1.

$\sim 0.55 - 0.60$ keV. The inner disc temperature decreased gradually from ~ 0.6 keV on 6 November 2019 to ~ 0.11 keV on 29 January 2020 (in HSS and HIMS). The photon index (Γ) in this phase decreased from 5.03 to 3.23, though similar variations (in the range of 3.17 – 4.97) were seen during the HSS in the declining phase of the outburst (blue circles in Fig. 5). During the HIMS and LHS (green squares and magenta diamonds in Fig. 5, respectively), the spectra became flat with Γ in the range of $\sim 1.68 - 2.62$. The diskbb normalization (N_{DBB}) varied in the range of $\sim 2700 - 3500$ in the SIMS and HSS. However, in the HIMS, we observed a higher value of N_{DBB} (> 8000).

Interestingly, we did not find any signature of the presence of iron emission line in the spectral residuals. Thus, we attempted to estimate the UL on the equivalent width (EW) of the Fe $K\alpha$ emission line at 6.4 keV. In the beginning, we added a narrow Gaussian line with fixed-line energy (at 6.2, 6.4, 6.5 and 6.7 keV) and line width (0.01, 0.05, 0.1, and 0.2 keV) to calculate the EW. We observed that if an iron line was present, it is most likely at ~ 6.4 keV, where the maximum value of EW was obtained for a line width of 0.2 keV. The UL on the EW of the iron emission line was 0.019 keV, 0.067 keV, 0.007 keV and $< 10^{-4}$ keV for SIMS, HSS, HIMS and LHS, respectively. While fitting the averaged spectra from the four spectral states, the UL on EW was estimated to be 0.020 keV, 0.091 keV, 0.031 keV and 0.002 keV, respectively.

Unabsorbed flux in 0.7–10 keV range (F_{tot}), estimated from the spectral fitting of the *NICER* observations, are shown in Fig. 6(a). Thermal (F_{disc}) and non-thermal Comptonized flux (F_{Compt}) are shown in panels (b) and (c) of Fig. 6, respectively. In Fig. 6(d) & (e), the thermal fraction (f_{disc}), and the non-thermal Comptonized fraction (f_{Compt}) are shown. The thermal and non-thermal fractions are defined as the ratio between F_{disc} & F_{tot} , and F_{Compt} & F_{tot} , respectively. In the rising phase of the outburst, the 0.7–10 keV unabsorbed total flux as well as the thermal multi-colour disk blackbody flux (F_{disc}) were increasing. The 0.7–10 keV unabsorbed source flux became maximum ($F_{\text{tot}} = 8.96 \times 10^{-9}$ erg cm $^{-2}$ s $^{-1}$) at the peak of the outburst on 6 November 2019 (MJD 58793.14). In the declining phase, we observed a monotonous decrease in F_{tot} and F_{disc} . Though the non-thermal Comptonized flux (F_{Compt}) also decreased during the declining phase, the variation was not as smooth as F_{tot} and F_{disc} . In the SIMS and the HSS (red & blue data points in the figure, respectively), the source flux in 0.7–10 keV energy band was dominated by the thermal disc flux. Particularly in the rising phase, the thermal fraction was very high at $f_{\text{disc}} > 0.7$ and decreased slowly to $f_{\text{disc}} \geq 0.6$ as the outburst progressed (HSS). In the HIMS, the Comptonized flux started to dominate with $f_{\text{Compt}} \geq 0.5$. In the LHS, however, only non-thermal Comptonized flux (f_{Compt}) was observed due to non-detection of thermal component. The best-fit parameters obtained from our spectral analysis are given in Table 1.

We attempted to fit the spectra by replacing diskbb model component with diskpnp model (Gierliński et al. 1999). The diskpnp component is an extension of diskbb model by incorporating corrections for the temperature distribution near the black hole by considering the torque-free inner-boundary condition. Results obtained by fitting data with absorbed diskpnp+nthcomp model are found to be comparable to that obtained for absorbed diskbb+nthcomp model. The variation of the maximum disc temperature (T_{max}) obtained from the diskpnp model are same as the inner disc temperature (T_{in}), obtained from the diskbb model, within uncertainties.

We also fitted the 0.5–10 keV *Swift*/XRT spectra from all 85 epochs of observation between 7 November 2019 and 30 March 2020 using the above model. The results obtained from the fitting

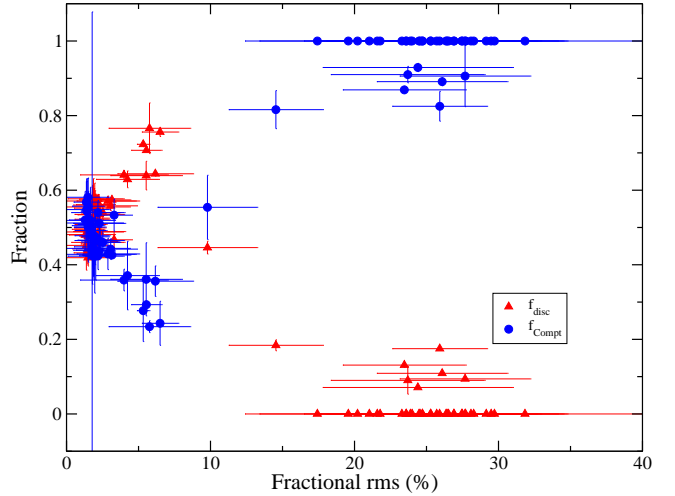


Figure 9. The thermal (disc) and non-thermal (Comptonized) emission fractions are plotted as a function of fractional rms amplitude (r). Red triangles and blue circles represent the thermal (f_{disc}) and Comptonized flux fraction (f_{Compt}), respectively.

are broadly similar to that obtained from the *NICER* observations, though the errors estimated from the fitting of *Swift*/XRT data were large. Therefore, we did not describe here in detail.

3.4 Evolution of Spectro-Temporal Properties

As described in the previous section, we classified the entire outburst into four different spectral states such as SIMS (rising phase - red triangles), HSS (declining phase - blue circles), HIMS (declining phase - green squares), and LHS (declining phase - magenta diamonds). The evolution of the source among these spectral states can also be recognized while studying the correlation between the observed spectral and timing properties. For this purpose, we generated the hardness-intensity diagram (HID) and rms-intensity diagram (RID). In Fig. 7 and Fig. 8, the HR (ratio between the count rates in 2–10 keV and 0.5–2 keV ranges) and the 0.01–50 Hz fractional rms amplitude are plotted as a function of the source count rate in 0.5–10 keV energy range, respectively.

From Fig. 7 & Fig. 8, we observed that the HR and rms were positively correlated with the source count rate during the SIMS in the rising phase (red triangles). In this phase of the outburst, the track of the source in the HID and RID was from left to right, as marked with red arrows in both the figures. In the HSS, the source intensity decreased gradually along with the decrease in HR and fractional rms amplitude values. The evolution track of the source in the HID and RID were in the opposite direction to that during the rising phase (SIMS) of the outburst (blue arrows in Fig. 7 & Fig. 8). This trend was clearly observed until 10 January 2020. Beyond 10 January 2020, the evolution track of the source was changed from left to right in the HID and RID (see Fig. 7 & Fig. 8). The HR and fractional rms amplitude started increasing rapidly with the decrease in source count rate as the source were in the HIMS (see Fig. 7 & Fig. 8). After 29 January 2020, the HR and fractional rms amplitude varied randomly as the count rate decreased further (see Fig. 7 & Fig. 8) when the source was in the LHS.

4 DISCUSSION

We present a detailed analysis of the spectral and timing properties of the 2019–2020 outburst of the recently discovered BHC MAXI J0637–430. We used a total of 88 epochs of *NICER* observations in 0.7 – 10 keV energy band and 85 observations with the *Swift*/XRT in the energy band of 0.5 – 10 keV. The spectra were fitted with a thermal blackbody and non-thermal Comptonized model. Among the total of 88 *NICER* observations, the thermal disc component was required in the first 54 observations. We found that the source evolved through SIMS → HSS → HIMS → LHS during the entire outburst.

4.1 Nature of the X-ray source

The nature of the compact object in MAXI J0637–430, though believed as a black hole, has not been confirmed yet. Based on the results obtained from a *NuSTAR* observation in 3 – 79 keV range on 5 November 2019, Tomsick et al. (2019) suggested that the system is a BHXR. As the mass of the compact object has not yet been estimated through the dynamical process and lack of clear signature of neutron star (NS) system such as pulsations and/or thermonuclear bursts, the nature of the compact object is unclear. Thus, we attempted to infer the nature of the compact object from the timing and spectral properties. We searched for the presence of high-frequency kHz QPOs, seen in several NSs (Di Salvo et al. 2001; van Doesburgh & van der Klis 2017; Bult et al. 2018; Méndez & Belloni 2021), in the PDS up to 1250 Hz. However, we did not find any signs of such features in the PDS. Absence of kHz QPOs, however, did not discard the compact object as an NS. The PDS showed that the power decreased rapidly in frequency > 10 Hz, which is consistent with the BHXR (Sunyaev & Revnivtsev 2000). Generally, the power diminishes in the frequency range of ~ 10 – 50 Hz for BHXR, while the NSXR shows variability up to as high as ~ 100 – 200 Hz. The evolution of HID and RID of MAXI J0637–430 is similar to that of other BHXR (Homan & Belloni 2005; Belloni et al. 2005; Remillard & McClintock 2006; Alabarta et al. 2020; Zhang et al. 2020). However, several NS binary systems, especially at low accretion rate, also follow a similar evolution track (Körding et al. 2008; Muñoz-Darias et al. 2011, 2014). The state transition track in low accreting NS is diagonal, while it is horizontal in the case of BH (Muñoz-Darias et al. 2014). Though *RXTE* and *NICER* operate in different energy ranges with certain overlap, for a given source, the HID and RID from both sets of instruments are similar (Alabarta et al. 2020). While comparing the evolution tracks of HID and RID of BHCs GX 339–4, MAXI J1727–203, MAXI J1348–630 (Belloni et al. 2005; Muñoz-Darias et al. 2014; Alabarta et al. 2020; Zhang et al. 2020) and MAXI J0637–430 (present work, see Fig. 7 and Fig. 8), it can be seen that the state transition track followed a horizontal path in case of all the sources. Similar evolution track of HID and RID as other BHCs and non-detection of any characteristics of neutrons stars such as pulsations, thermonuclear bursts and kHz QPOs in the PDS suggest that the X-ray source in the MAXI J0637–430 binary system is likely to be a BH.

The evolution of the spectral properties of MAXI J0637–430 is consistent with that of BH LMXB. Usually, the BH spectra contain an ultra-soft multi-colour blackbody component ($T \lesssim 1$ keV) and a power-law tail. However, the NS spectra contain a soft component that originates from the surface of the NS and a multi-colour disc blackbody component from the accretion disc along with Comptonized power-law tail (Fu & Taam 1990). In this work,

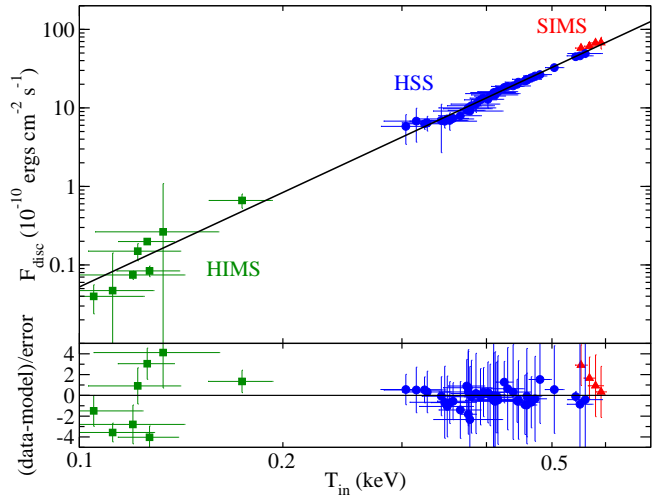


Figure 10. Disk blackbody flux (F_{disc}) is plotted as a function of inner disc temperature (T_{in}) in the upper panel. Solid black line represent $F_{\text{disc}} \sim T_{\text{in}}^4$ line. In the lower panel, residual is plotted. The colours and symbol correspond to the different spectral states of the source during the outburst as described in Fig. 1.

the 0.7 – 10 keV *NICER* spectra were fitted with a ultra-soft thermal component ($T_{\text{in}} \lesssim 0.6$ keV) and a power-law tail (see, Section 3.3), considering the compact object as a BH. In order to check the NS nature of the X-ray source in the binary, we carried out the spectral fitting of the data taken during the bright phase of the outburst with a more general NS model consisting of emission from the surface of the NS (bbodyrad), accretion disc (diskbb) along with the power-law continuum model (nthcomp). Parameters corresponding to temperatures of the NS surface and accretion disc, obtained from fitting the data with this NS specific model, are $kT_{\text{bbodyrad}} \sim 0.6 \pm 0.2 - 0.1 \pm 0.1$ keV and $T_{\text{in}} \sim 0.6 \pm 0.01 - 0.1 \pm 0.005$ keV, respectively. The normalization of the bbodyrad component was very low ($\sim 2.5 \pm 2$) compared to that of diskbb component (> 2500). Although the fitting was acceptable with a reduced $\chi^2 \sim 1$, it was clear that the thermal component corresponding to the emission from the NS surface was insignificant and not required. We also used F-test statistic to check if the second thermal component was required in the spectral fitting. The F-test rejected the probability of two thermal components in the spectra. Observed timing and spectral characteristics of MAXI J0637–430; therefore, suggest that the compact object is a black hole.

4.2 Evolution of the Outburst

An outburst is thought to be triggered by the sudden enhancement of the viscosity at the outer edge of the disc (Ebisawa et al. 1996). In the initial phase of the outburst, LHS is observed with a disc truncated at a large distance. In this state, the Comptonized emission dominates the spectrum with $F_{\text{Compt}} > 80\%$ (Remillard & McClintock 2006). As the outburst progresses, the disc emission starts to dominate, and the source moves through the HIMS, SIMS and HSS. The disc is observed to move closer to the BH in the rising phase of the outburst. The source entered the declining phase when the viscosity is turned off, and the matter supply is cut-off. As the disc is already formed, it is not easy to accrete the disc matter in the absence of viscosity (Roy & Chakrabarti 2017). The disc gets accreted slowly to the BH;

hence we see relatively long HSS and SIMS in the declining phase. Once the disc matter is accreted on to the BH, the source quickly evolves through the HIMS and LHS, as the supply of the matter has already been cut-off. This is why very short HIMS and LHS are observed in the declining phase of an X-ray outburst.

In the 2019–2020 outburst of MAXI J0637–430, the LHS and the HIMS were not observed. It is possible that the source moved quickly through the harder states (LHS and HIMS). However, this transition could not be investigated due to the lack of X-ray observations during this phase. The source was caught in SIMS with *NICER* only ~ 4 days prior to the peak of the outburst. After reaching the peak, the source entered the declining phase during which the X-ray intensity slowly decreased over the next ~ 65 days, which implies that nearly two months duration was required to drain the disc. As the matter supply was already cut-off and very little matter remained, the X-ray intensity suddenly dropped by ~ 10 times once the disc matter was drained. Then, the source quickly evolved through the HIMS and entered to a very low luminosity LHS.

Evolving type-C QPOs are known to be detected in the HIMS and LHS, whereas the sporadic type-A or type-B QPOs may be observed in the SIMS. However, no QPOs are observed in the HSS (Belloni et al. 2005; Remillard & McClintock 2006). The oscillation of the Compton cloud is believed to be responsible for the QPOs (Molteni et al. 1996; Titarchuk et al. 1998; Chakrabarti & Manickam 2000; Cabanac et al. 2010). It is well established that the Comptonized photons are responsible for the variability observed in the PDS and light curves (van der Klis 2004). In general, strong variability is observed in the LHS with fractional rms amplitude of $\sim 20 - 40\%$. In the HIMS and SIMS, fractional rms amplitudes of $10 - 20\%$ and $\sim 5 - 10\%$ are seen, respectively. However, in the HSS, weak variability with fractional rms amplitude of $< 5\%$ are observed (van der Klis 1994; Méndez & van der Klis 1997; Belloni et al. 2005). In the current outburst of MAXI J0637–430, weak variability is observed in the SIMS and HSS with fractional rms $r \leq 5\%$ (red and blue colour in Fig. 1). Strong variability are observed in the LHS and HIMS with $r > 20\%$ and $\sim 10 - 20\%$ (magenta and green colors in Fig. 1), respectively, as the Comptonized hard photons dominate these states. In Fig 9, we plot fractional rms amplitude as a function of the thermal and non-thermal fraction. From this figure, it is clear that strong variability is observed when the non-thermal fraction is higher, i.e., Comptonized photons dominate the total flux.

We tried to find the dependency of disc flux (F_{disc}) with the inner disc temperature (T_{in}). We fitted the distribution with a relation $F_{\text{disc}} \sim T_{\text{in}}^b$. The best-fit exponent is derived to be $b = 4.24 \pm 0.14$. This is higher than the theoretical value of $b = 4$. In the upper panel of Fig. 10, we show thermal disc flux (F_{disc}) as a function of inner disc temperature (T_{in}). The disc flux was fitted with $F_{\text{disc}} \sim T_{\text{in}}^4$ relation, and the residual is plotted in the lower panel of Fig. 10. The red triangles, blue circles and green diamonds represent data from the SIMS, HSS and HIMS, respectively. The solid black line represents the theoretical relation, $F_{\text{disc}} \sim T_{\text{in}}^4$. From Fig. 10, it can be seen that the observed disc flux was in agreement with the theoretical value in the HSS and SIMS. However, there was a deviation from the theoretical value in the HIMS when the disc flux was low. The $F_{\text{disc}} \sim T_{\text{in}}^4$ relation is predicted for a non-rotating black hole, assuming the inner edge and spectral hardening factor to remain constant (Gierliński & Done 2004). Therefore, the deviation in the HIMS could be due to the moving inner edge or change in the hardening factor or both (Dunn et al. 2011). Similar behaviour is also observed for other black hole X-ray binaries (Gierliński & Done 2004; Dunn et al. 2010, 2011).

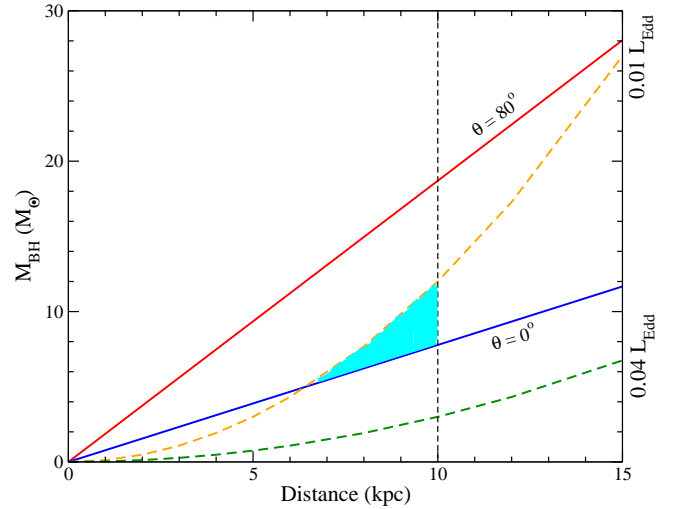


Figure 11. Mass-distance relation for MAXI J0637–430 is plotted assuming a non-rotating black hole. Red and blue solid lines correspond to the inclination angle $\theta = 80^\circ$ and $\theta = 0^\circ$, respectively. The orange dashed and green dashed curves show the mass-distance relation for $L_{\text{tr}}/L_{\text{Edd}} = 0.01$ and $L_{\text{tr}}/L_{\text{Edd}} = 0.04$, respectively. The shaded region is the common parameter space of $M_{\text{BH}} - d$, obtained from Equation 2 and Equation 3. The vertical dashed black line represent $d = 10$ kpc.

In our analysis, we did not detect any signature of the presence of the Fe $K\alpha$ emission line, which is very unusual. Thus, we calculated the UL on the EW of the Fe $K\alpha$ line in the *NICER* spectra. The UL was estimated to be 0.019 keV, 0.067 keV, 0.007 keV and $< 10^{-4}$ keV in the SIMS, HSS, HIMS and LHS, respectively. The averaged spectra from each of the four spectral states gives UL on the EW as 0.020 keV, 0.091 keV, 0.011 keV and 0.002 keV, respectively. From this, it is observed that a weak Fe line might be present in the spectra of HSS. Non-detection of Fe emission line could also be due to the short exposure time of *NICER* observations. In the case of 2018 outburst of MAXI J1813–095, the Fe $K\alpha$ line was not detected with the *NICER* observation with short exposure time ($\sim 1 - 2$ ks), but *NuSTAR* observation with a long exposure (~ 20 ks) detected a broad iron line (Jana et al. 2021). Indeed in the current outburst, Tomsick et al. (2019) observed an Fe $K\alpha$ line with the *NuSTAR* observation, which has long exposure. We also did not observe reflection hump in the spectra as it is expected in $\sim 15 - 40$ keV range (Fabian et al. 1989; Matt et al. 1991), which is outside of *NICER* energy range.

4.3 Estimation of mass and distance of MAXI J0637–430

In the softer spectral states (SIMS and HSS), the accretion flow is expected to be truncated at very close to the BH. During the SIMS and HSS of the outburst, the normalization (N_{DBB}) of the diskbb model did not vary much. It varied in the range of $\sim 2700 - 3500$ indicating that the inner edge (R_{in}) of the disc was remarkably stable in the SIMS and HSS (Ebisawa et al. 1993). We tried to constrain the mass and distance of the BH by equating R_{in} with the innermost stable circular orbit (ISCO). The normalization of the Diskbb model is given by, $N_{\text{DBB}} = (r_{\text{in}}/D_{10})^2 \cos \theta$, where r_{in} is apparent disc radius in km, D_{10} is the source distance in the unit of 10 kpc, and θ is the inclination angle. The inner edge of the disc (R_{in}) is given by, $R_{\text{in}} = \xi \kappa^2 r_{\text{in}}$, where $\xi = 0.41$ is correction factor

(Kubota et al. 1998), $\kappa = 1.7 - 2.0$ is the spectral hardening factor (Shimura & Takahara 1995). Using, $\kappa = 1.8$, we get,

$$R_{\text{in}} = (73 \pm 4)D_{10}(\cos \theta)^{-1/2}. \quad (1)$$

In our calculation, we used the mean value of $N_{\text{DBB}} = 3045 \pm 175$ from corresponding observed values during the SIMS and HSS. For a Schwarzschild black hole, $R_{\text{ISCO}} = 6r_g$, where r_g is gravitational radius. From these equations and assuming a non-rotating BH, we obtained the mass of the BH as,

$$M_{\text{BH}} = (8 \pm 1)D_{10}(\cos \theta)^{-1/2}M_{\odot}. \quad (2)$$

We plotted the mass-distance relation for MAXI J0637–430 in Fig. 11 assuming a non-rotating black hole, using Equation 2. Red and blue solid lines correspond to the inclination angle $\theta = 80^\circ$ and $\theta = 0^\circ$, respectively. From this, the M_{BH} should lie in the parameter space between these two line. However, M_{BH} is not well-constrained and depends on the source distance. Assuming the source distance, $d < 10$ kpc, the value of the mass of the BH would be $M_{\text{BH}} < 18 M_{\odot}$. The above calculation may not hold for a rotating BH, since, the diskbb model assumes a non-rotating BH.

To constrain the mass and distance of the BH better, we used spectral state transition luminosity relation (Maccarone 2003; Tetarenko et al. 2016). Empirically, soft-to-hard state transition luminosity (L_{tr}) is observed as,

$$L_{\text{tr}} \sim 0.01 - 0.04 L_{\text{Edd}}. \quad (3)$$

Recently, Jana et al. (2020) estimated the distance of MAXI J1348–630 using this relation. We calculated the state-transition luminosity (L_{tr}) from the unabsorbed flux obtained on 10 January 2020. In Fig. 11, the orange dashed and green dashed curves show the mass-distance relation for $L_{\text{tr}}/L_{\text{Edd}} = 0.01$ and $L_{\text{tr}}/L_{\text{Edd}} = 0.04$, respectively. The shaded region in Fig 11 shows the common parameter space of $M_{\text{BH}} - d$ obtained from Equation 2 and Equation 3. From this, we infer that the mass of the BH is in the range of $5 - 12 M_{\odot}$, for the source distance of $d < 10$ kpc. This mass-distance relation also infers that the source is located at a distance of $d > 6.5$ kpc (lower end of the shaded region in Fig. 11). However, our estimation of the mass, distance and inclination angle is based on the assumption of a non-rotating black hole. A more detailed optical study is required to estimate the distance and/or inclination angle of the source.

5 SUMMARY

We studied the 2019-2020 outburst of MAXI J0637–430 with *NICER* and *Swift* observations. Following are the key findings from this study.

(i) From the detailed timing and spectral studies, we conclude that the compact object in MAXI J0637–430 is likely to be a black hole.

(ii) We classified the outburst in four spectral states: SIMS, HSS, HIMS and LHS. The classification was done based on the evolution of the soft X-ray flux, hard X-ray flux, HR, HID and RID.

(iii) No QPOs were observed during the outburst.

(iv) Weak variability (fractional variability amplitude, $r < 5\%$) are observed in the SIMS and HSS. In the HIMS and LHS, however, strong variability were observed with $r > 20\%$. Comptonized

photons are responsible for the observed variability in the PDS and light curves.

(v) The 0.7–10 keV *NICER* spectra were fitted with a composite model consisting of disk blackbody and nthcomp, along with the interstellar absorption. Spectra obtained from 54 observations from the beginning when the source was in SIMS, HSS and HIMS, fitted well with this model. However, the thermal disc component was undetectable in the spectral fitting in the LHS.

(vi) Thermal disc flux and inner disc temperature followed the theoretical relation of $F_{\text{disc}} \sim T_{\text{in}}^4$ in the HSS and SIMS. A deviation of the relation is observed in the HIMS. Moving inner edge or change of spectral hardening factor could be responsible for that.

(vii) Assuming a non-rotating BH, we estimated the mass of the BH as $5 - 12 M_{\odot}$ for a distance of $d < 10$ kpc.

(viii) No signature of Fe emission line was seen. This could be due to the short exposure time of *NICER* observations.

ACKNOWLEDGEMENTS

We acknowledge the reviewer for his/her helpful comments/suggestions which improved the paper. We sincerely thank Jon M. Miller and Zaven Arzoumanian for their constructive suggestions on the paper. This research has made use of data and/or software provided by the High Energy Astrophysics Science Archive Research Center (HEASARC), which is a service of the Astrophysics Science Division at NASA/GSFC and the High Energy Astrophysics Division of the Smithsonian Astrophysical Observatory. This work was made use of XRT data supplied by the UK Swift Science Data Centre at the University of Leicester, UK. Work at Physical Research Laboratory, Ahmedabad, is funded by the Department of Space, Government of India.

DATA AVAILABILITY

We used archival data of *Swift*, and *NICER* observatories for this work.

REFERENCES

- Alabarta K., et al., 2020, *MNRAS*, **497**, 3896
 Arnaud K. A., 1996, in Jacoby G. H., Barnes J., eds, *Astronomical Society of the Pacific Conference Series Vol. 101, Astronomical Data Analysis Software and Systems V*. p. 17
 Belloni T., Psaltis D., van der Klis M., 2002, *ApJ*, **572**, 392
 Belloni T., Homan J., Casella P., van der Klis M., Nespoli E., Lewin W. H. G., Miller J. M., Méndez M., 2005, *A&A*, **440**, 207
 Bult P., et al., 2018, *ApJ*, **860**, L9
 Cabanac C., Henri G., Petrucci P. O., Malzac J., Ferreira J., Belloni T. M., 2010, *MNRAS*, **404**, 738
 Casella P., Belloni T., Stella L., 2005, *ApJ*, **629**, 403
 Chakrabarti S. K., Manickam S. G., 2000, *ApJ*, **531**, L41
 Chakrabarti S., Titarchuk L. G., 1995, *ApJ*, **455**, 623
 Chen W., Shrader C. R., Livio M., 1997, *ApJ*, **491**, 312
 Di Salvo T., Méndez M., van der Klis M., Ford E., Robba N. R., 2001, *ApJ*, **546**, 1107
 Done C., Gierliński M., Kubota A., 2007, *A&ARv*, **15**, 1
 Dunn R. J. H., Fender R. P., Körding E. G., Belloni T., Cabanac C., 2010, *MNRAS*, **403**, 61
 Dunn R. J. H., Fender R. P., Körding E. G., Belloni T., Merloni A., 2011, *MNRAS*, **411**, 337
 Ebisawa K., Makino F., Mitsuda K., Belloni T., Cowley A. P., Schmidtke P. C., Treves A., 1993, *ApJ*, **403**, 684

- Ebisawa K., Titarchuk L., Chakrabarti S. K., 1996, *PASJ*, **48**, 59
- Evans P. A., et al., 2009, *MNRAS*, **397**, 1177
- Fabian A. C., Rees M. J., Stella L., White N. E., 1989, *MNRAS*, **238**, 729
- Fender R., Belloni T., 2004, *ARA&A*, **42**, 317
- Fu A., Taam R. E., 1990, *ApJ*, **353**, 205
- Gendreau K. C., Arzoumanian Z., Okajima T., 2012, in Takahashi T., Murray S. S., den Herder J.-W. A., eds, *Society of Photo-Optical Instrumentation Engineers (SPIE) Conference Series Vol. 8443, Space Telescopes and Instrumentation 2012: Ultraviolet to Gamma Ray*. p. 844313, doi:10.1117/12.926396
- Gierliński M., Done C., 2004, *MNRAS*, **347**, 885
- Gierliński M., Zdziarski A. A., Poutanen J., Coppi P. S., Ebisawa K., Johnson W. N., 1999, *MNRAS*, **309**, 496
- HI4PI Collaboration et al., 2016, *A&A*, **594**, A116
- Haardt F., Maraschi L., 1993, *ApJ*, **413**, 507
- Homan J., Belloni T., 2005, *Ap&SS*, **300**, 107
- Homan J., Wijnands R., van der Klis M., Belloni T., van Paradijs J., Klein-Wolt M., Fender R., Méndez M., 2001, *ApJS*, **132**, 377
- Jaisawal G. K., et al., 2019, *ApJ*, **885**, 18
- Jana A., Debnath D., Chakrabarti S. K., Mondal S., Molla A. A., 2016, *ApJ*, **819**, 107
- Jana A., Debnath D., Chatterjee D., Chatterjee K., Chakrabarti S. K., Naik S., Bhowmick R., Kumari N., 2020, *ApJ*, **897**, 3
- Jana A., et al., 2021, *Research in Astronomy and Astrophysics*, in Press.,
- Kennea J. A., et al., 2019, *The Astronomer's Telegram*, **13257**, 1
- Körding E., Rupen M., Knigge C., Fender R., Dhawan V., Templeton M., Muxlow T., 2008, *Science*, **320**, 1318
- Kubota A., Tanaka Y., Makishima K., Ueda Y., Dotani T., Inoue H., Yamaoka K., 1998, *PASJ*, **50**, 667
- Li K.-L., Kong A. K. H., 2019, *The Astronomer's Telegram*, **13276**, 1
- Maccarone T. J., 2003, *A&A*, **409**, 697
- Makishima K., Maejima Y., Mitsuda K., Bradt H. V., Remillard R. A., Tuohy I. R., Hoshi R., Nakagawa M., 1986, *ApJ*, **308**, 635
- Matt G., Perola G. C., Piro L., 1991, *A&A*, **247**, 25
- Méndez M., Belloni T. M., 2021, *High-Frequency Variability in Neutron-Star Low-Mass X-ray Binaries*. pp 263–331, doi:10.1007/978-3-662-62110-3_6
- Méndez M., van der Klis M., 1997, *ApJ*, **479**, 926
- Mitsuda K., et al., 1984, *PASJ*, **36**, 741
- Molteni D., Sponholz H., Chakrabarti S. K., 1996, *ApJ*, **457**, 805
- Muñoz-Darias T., Motta S., Belloni T. M., 2011, *MNRAS*, **410**, 679
- Muñoz-Darias T., Fender R. P., Motta S. E., Belloni T. M., 2014, *MNRAS*, **443**, 3270
- Murata K. L., et al., 2019, *The Astronomer's Telegram*, **13292**, 1
- Nandi A., Debnath D., Mandal S., Chakrabarti S. K., 2012, *A&A*, **542**, A56
- Negoro H., et al., 2019, *The Astronomer's Telegram*, **13256**, 1
- Novikov I. D., Thorne K. S., 1973, in *Black Holes (Les Astres Occlus)*. pp 343–450
- Nowak M. A., 2000, *MNRAS*, **318**, 361
- Prigozhin G., et al., 2012, in Holland A. D., Beletic J. W., eds, *Society of Photo-Optical Instrumentation Engineers (SPIE) Conference Series Vol. 8453, High Energy, Optical, and Infrared Detectors for Astronomy V*. p. 845318, doi:10.1117/12.926667
- Remillard R. A., McClintock J. E., 2006, *ARA&A*, **44**, 49
- Remillard R., Pasham D., Gendreau K., Arzoumanian Z., Homan J., Altamirano D., Steiner J., 2020, *The Astronomer's Telegram*, **13427**, 1
- Roy A., Chakrabarti S. K., 2017, *MNRAS*, **472**, 4689
- Russell T. D., Miller-Jones J. C. A., Sivakoff G. R., Tetarenko A. J., 2019, *The Astronomer's Telegram*, **13275**, 1
- Shakura N. I., Sunyaev R. A., 1973, *A&A*, **500**, 33
- Shimura T., Takahara F., 1995, *ApJ*, **445**, 780
- Strader J., Aydi E., Sokolovsky K., Shishkovsky L., 2019, *The Astronomer's Telegram*, **13260**, 1
- Sunyaev R., Revnivtsev M., 2000, *A&A*, **358**, 617
- Sunyaev R. A., Titarchuk L. G., 1980, *A&A*, **500**, 167
- Sunyaev R. A., Titarchuk L. G., 1985, *A&A*, **143**, 374
- Tetarenko B. E., Sivakoff G. R., Heinke C. O., Gladstone J. C., 2016, *ApJS*, **222**, 15
- Thomas N. T., Gudennavar S. B., Misra R., Bubbly S. G., 2019, *The Astronomer's Telegram*, **13296**, 1
- Titarchuk L., 1994, *ApJ*, **434**, 570
- Titarchuk L., Lapidus I., Muslimov A., 1998, *ApJ*, **499**, 315
- Tomsick J. A., et al., 2019, *The Astronomer's Telegram*, **13270**, 1
- Verner D. A., Ferland G. J., Korista K. T., Yakovlev D. G., 1996, *ApJ*, **465**, 487
- White N. E., Nagase F., Parmar A. N., 1995, in *X-ray Binaries*. pp 1–57
- Wilms J., Allen A., McCray R., 2000, *ApJ*, **542**, 914
- Zdziarski A. A., Zycki P. T., Svensson R., Boldt E., 1993, *ApJ*, **405**, 125
- Zhang L., et al., 2020, *MNRAS*, **499**, 851
- Życki P. T., Done C., Smith D. A., 1999, *MNRAS*, **309**, 561
- van der Klis M., 1989, *ARA&A*, **27**, 517
- van der Klis M., 1994, *ApJS*, **92**, 511
- van der Klis M., 2000, *ARA&A*, **38**, 717
- van der Klis M., 2004, arXiv e-prints, pp astro-ph/0410551

This paper has been typeset from a \LaTeX file prepared by the author.

Table 1. Best-fit parameters obtained from spectral fitting of data obtained from the *NICER* observations of MAXI J0637–430 during its 2019-2020 outburst

Obs ID	UT Date (yyyy-mm-dd)	Exp (s)	Date (MJD)	Count Rate (Count s ⁻¹)	DBB Flux ^a	PL Flux ^a	T_{in} (keV)	N_{DBB}	Γ	χ^2/dof
2200950101	2019-11-03	1080	58790.92	5843	57.82 ± 0.71	22.13 ± 1.75	0.55 ± 0.02	2969 ± 88	5.03 ± 0.07	540/ 519
2200950102	2019-11-04	6698	58791.50	6288	61.06 ± 1.15	25.20 ± 1.02	0.57 ± 0.01	3048 ± 115	4.67 ± 0.05	718/ 696
2200950103	2019-11-05	571	58792.50	6486	67.29 ± 1.15	20.50 ± 1.16	0.58 ± 0.01	2973 ± 102	4.71 ± 0.09	512/ 497
2200950104	2019-11-06	334	58793.14	6533	67.77 ± 2.25	21.83 ± 1.83	0.60 ± 0.01	3032 ± 93	3.53 ± 0.04	528/ 464
2200950107	2019-11-12	591	58799.63	5280	49.27 ± 3.53	27.19 ± 1.96	0.56 ± 0.03	3082 ± 106	3.23 ± 0.08	509/ 538
2200950108	2019-11-13	1821	58800.60	5108	46.02 ± 2.26	25.96 ± 2.94	0.55 ± 0.02	2991 ± 134	3.86 ± 0.06	415/ 409
2200950109	2019-11-14	3760	58801.47	4946	44.86 ± 3.15	25.03 ± 1.07	0.54 ± 0.04	2801 ± 152	4.50 ± 0.07	521/ 558
2200950111	2019-11-21	18	58808.66	3715	32.59 ± 2.18	19.18 ± 0.92	0.50 ± 0.01	2954 ± 244	3.17 ± 0.04	589/ 568
2200950112	2019-11-26	6736	58813.39	3252	26.58 ± 0.80	19.65 ± 1.71	0.48 ± 0.02	3160 ± 122	4.06 ± 0.04	613/ 622
2200950113	2019-11-27	1213	58814.77	3113	25.51 ± 1.52	19.16 ± 1.58	0.47 ± 0.02	3321 ± 123	3.84 ± 0.06	494/ 471
2200950114	2019-11-28	1936	58815.48	3034	24.22 ± 0.74	19.17 ± 1.36	0.47 ± 0.01	3044 ± 423	4.26 ± 0.07	483/ 496
2200950115	2019-11-29	1962	58816.55	2906	23.13 ± 1.67	19.67 ± 1.30	0.46 ± 0.02	2774 ± 259	4.85 ± 0.07	519/ 481
2200950116	2019-11-30	2274	58817.61	2823	22.44 ± 0.88	19.13 ± 1.23	0.46 ± 0.01	2917 ± 231	4.79 ± 0.06	515/ 478
2200950117	2019-12-01	1778	58818.45	2748	22.08 ± 0.64	19.14 ± 1.21	0.46 ± 0.01	2998 ± 134	4.67 ± 0.09	479/ 461
2200950118	2019-12-02	743	58819.41	2678	21.27 ± 1.21	15.65 ± 2.01	0.45 ± 0.02	3094 ± 394	4.51 ± 0.06	402/ 402
2200950119	2019-12-03	2892	58820.51	2586	19.99 ± 0.72	15.57 ± 1.58	0.44 ± 0.01	3040 ± 412	4.39 ± 0.07	564/ 504
2200950120	2019-12-05	616	58822.19	2478	19.04 ± 0.77	13.92 ± 2.06	0.44 ± 0.02	2747 ± 212	4.51 ± 0.09	352/ 385
2200950121	2019-12-06	1908	58823.59	2383	18.78 ± 1.35	13.81 ± 2.12	0.43 ± 0.02	3332 ± 141	4.07 ± 0.04	367/ 354
2200950122	2019-12-07	1795	58824.53	2311	18.20 ± 0.86	13.41 ± 1.37	0.43 ± 0.01	3383 ± 258	3.91 ± 0.07	441/ 409
2200950123	2019-12-08	1243	58825.80	2214	16.09 ± 0.87	13.05 ± 1.58	0.42 ± 0.02	2926 ± 122	4.50 ± 0.08	407/ 403
2200950124	2019-12-09	2140	58826.52	2156	15.78 ± 1.49	12.38 ± 1.31	0.41 ± 0.02	2871 ± 103	4.61 ± 0.09	442/ 432
2200950125	2019-12-10	869	58827.56	2076	15.68 ± 2.07	12.28 ± 2.11	0.41 ± 0.03	2893 ± 96	4.05 ± 0.05	413/ 366
2200950126	2019-12-11	1412	58828.65	2039	15.62 ± 1.66	11.73 ± 1.90	0.41 ± 0.02	2701 ± 91	5.00 ± 0.03	410/ 368
2200950127	2019-12-12	1247	58829.14	2000	14.64 ± 0.79	11.71 ± 1.29	0.41 ± 0.03	3075 ± 136	4.62 ± 0.07	344/ 340
2200950128	2019-12-13	2146	58830.33	1924	15.21 ± 0.84	11.17 ± 1.38	0.41 ± 0.03	2901 ± 79	4.30 ± 0.06	315/ 324
2200950129	2019-12-14	3013	58831.29	1896	14.16 ± 1.74	11.06 ± 1.58	0.41 ± 0.02	2997 ± 102	5.02 ± 0.04	407/ 383
2200950130	2019-12-15	2077	58832.61	1853	12.86 ± 2.91	11.61 ± 1.38	0.40 ± 0.02	2972 ± 145	4.51 ± 0.03	409/ 392
2200950131	2019-12-16	1921	58833.45	1793	13.31 ± 1.35	11.59 ± 1.47	0.40 ± 0.02	3210 ± 209	4.51 ± 0.06	410/ 395
2200950132	2019-12-17	1373	58834.48	1743	12.66 ± 2.10	11.56 ± 1.76	0.39 ± 0.02	3066 ± 123	4.77 ± 0.05	397/ 356
2200950133	2019-12-19	1338	58836.42	1673	11.19 ± 2.40	11.19 ± 2.20	0.39 ± 0.03	2759 ± 140	4.94 ± 0.06	367/ 340
2200950135	2019-12-22	999	58839.22	1530	10.64 ± 2.19	10.27 ± 2.06	0.38 ± 0.03	3469 ± 356	4.27 ± 0.08	330/ 314
2200950136	2019-12-23	759	58840.06	1507	10.01 ± 1.40	10.46 ± 1.77	0.38 ± 0.04	2872 ± 292	4.73 ± 0.10	365/ 340
2200950137	2019-12-24	854	58841.09	1462	9.77 ± 0.96	10.07 ± 1.68	0.38 ± 0.03	2843 ± 311	4.97 ± 0.08	381/ 348
2200950138	2019-12-25	954	58842.12	1428	9.30 ± 0.12	10.02 ± 1.51	0.37 ± 0.02	3118 ± 193	4.65 ± 0.14	371/ 340
2200950139	2019-12-26	963	58843.16	1398	9.12 ± 0.47	9.976 ± 1.994	0.38 ± 0.04	3202 ± 90	4.55 ± 0.10	317/ 302
2200950140	2019-12-27	903	58844.32	1356	9.49 ± 0.35	9.525 ± 0.649	0.38 ± 0.01	2883 ± 213	4.35 ± 0.07	471/ 447
2200950142	2019-12-29	1076	58846.66	1275	7.95 ± 0.60	9.976 ± 1.322	0.37 ± 0.03	3248 ± 141	4.49 ± 0.05	385/ 332
2200950144	2020-01-01	1726	58849.23	1197	7.35 ± 0.74	9.715 ± 1.108	0.36 ± 0.01	3375 ± 293	4.62 ± 0.11	469/ 372
2200950145	2020-01-02	1873	58850.26	1171	6.93 ± 1.73	9.599 ± 1.034	0.35 ± 0.02	2998 ± 144	4.64 ± 0.11	402/ 356
2200950146	2020-01-03	1092	58851.23	1143	7.24 ± 0.58	8.778 ± 1.506	0.35 ± 0.03	3440 ± 196	4.80 ± 0.14	348/ 318
2200950147	2020-01-04	1333	58852.46	1106	6.77 ± 1.24	8.075 ± 1.244	0.35 ± 0.04	2983 ± 144	4.93 ± 0.12	370/ 325
2200950148	2020-01-05	1166	58853.49	1093	6.91 ± 4.21	7.040 ± 1.417	0.34 ± 0.02	3361 ± 121	4.50 ± 0.18	326/ 320
2200950149	2020-01-06	1091	58854.65	1069	6.44 ± 1.36	6.975 ± 1.145	0.33 ± 0.03	2910 ± 74	4.65 ± 0.19	366/ 326
2200950151	2020-01-08	2725	58856.59	1020	6.27 ± 0.95	7.374 ± 0.733	0.32 ± 0.02	3136 ± 92	4.63 ± 0.10	372/ 387
2200950152	2020-01-09	1493	58857.40	1008	6.76 ± 3.12	7.094 ± 1.293	0.31 ± 0.03	2925 ± 110	4.33 ± 0.06	391/ 372
2200950153	2020-01-10	991	58858.37	984	5.82 ± 2.38	6.651 ± 0.483	0.30 ± 0.02	3276 ± 169	4.16 ± 0.10	381/ 356
2200950154	2020-01-14	503	58862.85	133	0.66 ± 0.13	0.822 ± 0.131	0.17 ± 0.02	10446 ± 799	2.38 ± 0.12	192/ 187
2200950155	2020-01-21	1107	58869.74	142	0.26 ± 0.82	1.173 ± 0.094	0.13 ± 0.03	10639 ± 1494	1.91 ± 0.07	317/ 331
2200950156	2020-01-23	2283	58871.58	104	0.15 ± 0.03	0.991 ± 0.122	0.12 ± 0.02	15083 ± 2212	1.89 ± 0.05	364/ 401
2200950157	2020-01-24	2419	58872.12	86.4	0.12 ± 0.01	0.937 ± 0.093	0.13 ± 0.01	9525 ± 1283	1.88 ± 0.04	400/ 412
2200950158	2020-01-25	908	58873.19	70.4	0.07 ± 0.01	0.718 ± 0.085	0.12 ± 0.02	10751 ± 3212	1.81 ± 0.06	239/ 258
2200950159	2020-01-26	2511	58874.61	61.8	0.05 ± 0.02	0.475 ± 0.121	0.11 ± 0.02	13211 ± 2539	1.85 ± 0.09	410/ 394
2200950160	2020-01-28	1258	58876.36	47.9	0.08 ± 0.01	0.686 ± 0.112	0.13 ± 0.01	8477 ± 1677	1.83 ± 0.05	324/ 281
2200950161	2020-01-29	1444	58877.58	29.7	0.03 ± 0.01	0.514 ± 0.078	0.11 ± 0.02	14928 ± 2823	1.75 ± 0.07	316/ 267
2200950162	2020-01-30	1356	58878.42	27.7	–	0.515 ± 0.049	–	–	1.89 ± 0.13	291/ 261

Table 1 – *continued* Best-fit parameters obtained from spectral fitting of data obtained from the *NICER* observations of MAXI J0637–430 during its 2019-2020 outburst

Obs ID	UT Date (yyyy-mm-dd)	Exp (s)	Date (MJD)	Count Rate (Count s ⁻¹)	DBB Flux ^a	PL Flux ^a	T_{in} (keV)	N_{DBB}	Γ	χ^2/dof
2200950163	2020-01-31	2874	58879.55	23.4	–	0.512 ± 0.043	–	–	1.88 ± 0.09	367/356
2200950164	2020-02-01	6938	58880.59	21.6	–	0.282 ± 0.081	–	–	1.84 ± 0.10	541/484
2200950165	2020-02-02	4619	58881.39	18.4	–	0.338 ± 0.042	–	–	1.88 ± 0.15	383/351
2200950166	2020-02-03	1563	58882.43	16.2	–	0.279 ± 0.038	–	–	1.86 ± 0.10	283/245
2200950167	2020-02-04	1728	58883.72	13.9	–	0.287 ± 0.027	–	–	1.78 ± 0.09	189/220
2200950168	2020-02-05	683	58884.11	11.0	–	0.022 ± 0.002	–	–	1.84 ± 0.10	541/498
2200950169	2020-02-06	1314	58885.33	13.9	–	0.031 ± 0.003	–	–	1.65 ± 0.12	271/264
2200950170	2020-02-07	629	58886.63	9.1	–	0.015 ± 0.004	–	–	1.94 ± 0.08	102/96
2200950171	2020-02-08	912	58887.40	11.7	–	0.021 ± 0.002	–	–	2.07 ± 0.04	197/173
2200950173	2020-02-10	1285	58889.61	11.5	–	0.023 ± 0.004	–	–	1.84 ± 0.23	216/183
2200950174	2020-02-11	884	58890.81	10.8	–	0.021 ± 0.003	–	–	1.86 ± 0.27	144/137
2200950175	2020-02-13	934	58892.10	9.4	–	0.018 ± 0.003	–	–	1.92 ± 0.18	127/136
2200950176	2020-02-14	1550	58893.55	9.1	–	0.018 ± 0.002	–	–	1.89 ± 0.14	155/179
2200950177	2020-02-16	1392	58895.68	8.2	–	0.016 ± 0.002	–	–	1.97 ± 0.18	179/158
2200950178	2020-02-17	233	58896.31	8.0	–	0.016 ± 0.003	–	–	1.82 ± 0.19	34/39
2200950181	2020-02-20	777	58899.73	6.2	–	0.011 ± 0.003	–	–	2.22 ± 0.19	61/50
2200950182	2020-02-21	1129	58900.39	7.2	–	0.016 ± 0.002	–	–	1.68 ± 0.21	111/105
2200950183	2020-02-22	1391	58901.04	7.0	–	0.014 ± 0.002	–	–	1.84 ± 0.14	131/160
2200950184	2020-02-23	1538	58902.17	6.3	–	0.012 ± 0.003	–	–	1.95 ± 0.14	125/141
2200950185	2020-02-24	1035	58903.59	5.0	–	0.009 ± 0.003	–	–	1.88 ± 0.09	239/224
2200950186	2020-02-25	842	58904.31	5.2	–	0.009 ± 0.002	–	–	2.46 ± 0.12	80/70
2200950187	2020-02-27	1352	58906.07	5.1	–	0.009 ± 0.002	–	–	2.16 ± 0.15	135/97
2200950188	2020-02-28	1934	58907.21	5.2	–	0.009 ± 0.001	–	–	1.94 ± 0.13	127/128
2200950189	2020-02-29	1588	58908.11	5.4	–	0.010 ± 0.002	–	–	1.87 ± 0.13	56/53
3200950101	2020-03-01	1230	58909.15	4.2	–	0.007 ± 0.001	–	–	2.24 ± 0.16	134/111
3200950102	2020-03-02	1610	58910.35	4.7	–	0.008 ± 0.002	–	–	2.02 ± 0.07	138/121
3200950103	2020-03-03	1085	58911.57	4.4	–	0.008 ± 0.002	–	–	2.12 ± 0.11	92/91
3200950104	2020-03-04	231	58912.51	4.1	–	0.008 ± 0.003	–	–	2.04 ± 0.10	194/166
3200950105	2020-03-05	287	58913.09	3.9	–	0.007 ± 0.002	–	–	2.06 ± 0.09	28/33
3200950108	2020-03-16	997	58924.21	2.9	–	0.007 ± 0.002	–	–	1.86 ± 0.11	27/32
3200950109	2020-03-22	947	58930.51	2.4	–	0.004 ± 0.001	–	–	1.91 ± 0.10	51/57
3200950110	2020-03-24	1370	58933.02	2.3	–	0.004 ± 0.002	–	–	2.21 ± 0.06	66/55
3200950111	2020-04-08	1240	58947.09	1.5	–	0.002 ± 0.001	–	–	2.62 ± 0.09	55/45

^a Fluxes are in the unit of 10⁻¹⁰ erg cm⁻² s⁻¹.

Errors are quoted at 90% confidence.